Metals and Materials International (2020) 26:1295–1305
https://doi.org/10.1007/s12540-019-00392-2

Microstructural Characterization and Softening Mechanism of Ultra-Low Carbon Steel and the Control Strategy in Compact Strip Production Process

Bo Jiang[1] · Xuewen Hu[1,2] · Guoning He[1] · Huan Peng[2] · Haibo Wang[1] · Yazheng Liu[1]

Received: 24 June 2019 / Accepted: 21 July 2019 / Published online: 30 July 2019

Abstract
In this paper, the microstructures and properties of hot rolled ultra-low carbon steel sheet produced by different compact strip production (CSP) processes were investigated. The softening mechanism was also discussed and the control strategy was proposed in order to obtain optimum properties. Result showed that the average ferrite grain sizes of austenite rolling sheet and multiphase rolling sheet were 31.0 μm and 74.6 μm, respectively. The sheet after austenite rolling had a slightly higher yield and tensile strength while had a 6.3% higher elongation than that of the sheet after multiphase rolling. The higher dislocation in the sheet after multiphase rolling increased the strength while decreased the elongation. The softening mechanism of the sheet after multiphase rolling was the coarsening of ferrite grain. The combined role of {001} and {111} orientation resulted in a slight increase of the r and $\bar{r}$ value in the sheet after multiphase rolling. It was a wise choice to conduct rolling at the Ac_1 temperature in CSP process to increase the grain size and decrease the dislocation density. Then, the strength of the sheets could be further reduced and the elongation could also be improved.

Keywords CSP · Ultra-low carbon steel · Softening mechanism · EBSD · Yield strength

1 Introduction

CSP process has been widely built in the steel mill plant over years for plenty of advantages as been evidenced before [1–4]. A lot of high strength hot rolled steel sheets could be easily produced in CSP process due to grain boundary strengthening and precipitation strengthening. However, the current products of CSP process can not satisfy the requirements of higher formability and thinner steel sheet which has a wider market and better price. Consequently, it is urging to develop new CSP process or optimize the current process to produce the steel sheet with lower strength.

Many researchers have focused on the researches to get optimization of CSP process parameters, especially on the flow stress, recrystallization behavior, microstructures and properties after rolling in single ferrite region [5–9]. Jeong investigated the effect of hot-rolling temperature on cold rolled microstructure and texture of an IF steel and found that the texture of hot-rolled steel sheet has a substantial influence on the textural evolution of the cold-rolled and annealed steel sheets [9]. Liu reported the deformation microstructure of various warm rolled steels while the deformation temperature was in single ferrite region [10]. Barnett presented a lot of researches on the effect of rolling temperature in ferrite region on the microstructures and properties of steels with different compositions [6, 7]. By reviewing the related literatures before, it could be concluded that most researches mainly focused on the microstructural characterization and properties of steels rolled in single ferrite region. Few reported the softening mechanism of steel sheet, especially when the sheet was rolled in multiphase region.

In this paper, the microstructures and properties of hot rolled ultra-low carbon steel sheet produced by CSP processes of austenite rolling and multiphase rolling were compared. The softening mechanism was also discussed and the

✉ Bo Jiang
jiangbo@ustb.edu.cn

✉ Yazheng Liu
lyzh@ustb.edu.cn

[1] School of Materials Science and Engineering, University of Science and Technology Beijing, Beijing 100083, China

[2] Technology Center, Maanshan Iron & Steel Co., Maanshan 243002, China

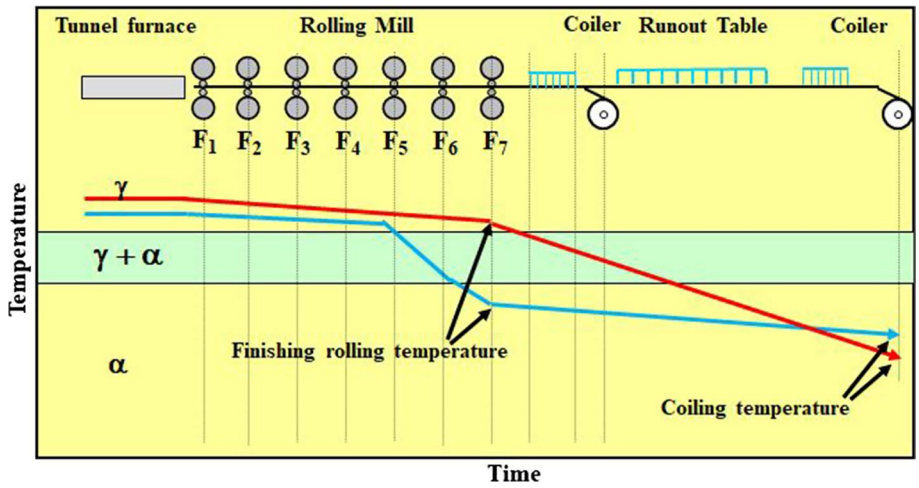

Fig. 1 The schematic process route of different CSP processes

Table 1 Rolling and coiling temperatures of different processes (°C)

No	F_1	F_2	F_3	F_4	F_5	F_6	F_7	Finish rolling temperature	Coiling temperature
No. 1	1061	1034	1012	990	963	934	903	891	609
No. 2	1018	982	963	935	902	869	833	806	703

control strategy was proposed in order to obtain optimum properties.

2 Experimental Procedures

2.1 Materials and Processes

The experimental steel was firstly continuous casted as a hot rectangular slab with the length of 300 mm, the width of 200 mm and the thickness of 50 mm by the CSP process in a steel mill. Next to the continuous casting was the heating process in the tunnel furnace in which the temperature could be adjusted. After that, the slab was roughing rolled and finishing rolled in a 7-stand tandem hot mill followed by cooling and coiling processes. The whole schematic process route was shown in Fig. 1. The thickness of the final hot sheet was 4.0 mm. The chemical composition of the investigated steel was determined as 0.005C-0.012Si-0.11Mn-0.014P-0.004S and was Fe balanced. Two different rolling processes of CSP can be seen in Fig. 1. For the process shown as the red line in the figure, the rolling temperatures of the whole 7-stand rolling process were in the austenite region. For the process shown in the blue line, the rolling temperature of first several stands fell into the austenite region while that of the following several stands may be in the two phase region or ferrite region. The coiling temperatures of different processes were also different and that of the latter one was much higher. The rolling temperatures at different stands and the coiling temperatures of different processes were shown in Table 1. Here the rolling temperatures were measured online before the slab entered each stand. The processes No. 1 and No. 2 were named as austenite rolling and multiphase rolling, respectively.

3 Properties Tests and Microstructural Investigation

Specimens for the tensile tests with 50 mm gauge length, 25 mm width, 4.0 mm thickness and 300 mm whole length were machined from the hot rolled steel coils. Tensile strength, yield strength and elongation were obtained according to GB/T 228-2010 [11]. The average plastic strain ratio $\bar{r}$ value was calculated using the equation $(r_0+2r_{45}+r_{90})/4$. Here, r_0, r_{45}, and r_{90} correspond to the r value determined in the direction of 0, 45, and 90 deg to the rolling direction, respectively. The anisotropic coefficient Δr value was obtained by using the equation $(r_0+r_{90})/2-r_{45}$.

The microstructures of the sheet were observed by OM (optical microscope) in normal direction (ND), transverse direction (TD) and rolling direction (RD). Samples were taken at the width of 1/2 of the hot rolled sheets. Transmission electron microscopy (TEM) (model: JEM-2100 (HR)) analysis was also performed to investigate the deformation dislocation density on the thin foil specimens and precipitates on carbon extraction replicas. To prepare thin foil specimens, slices of about 300 μm in thickness were cut by

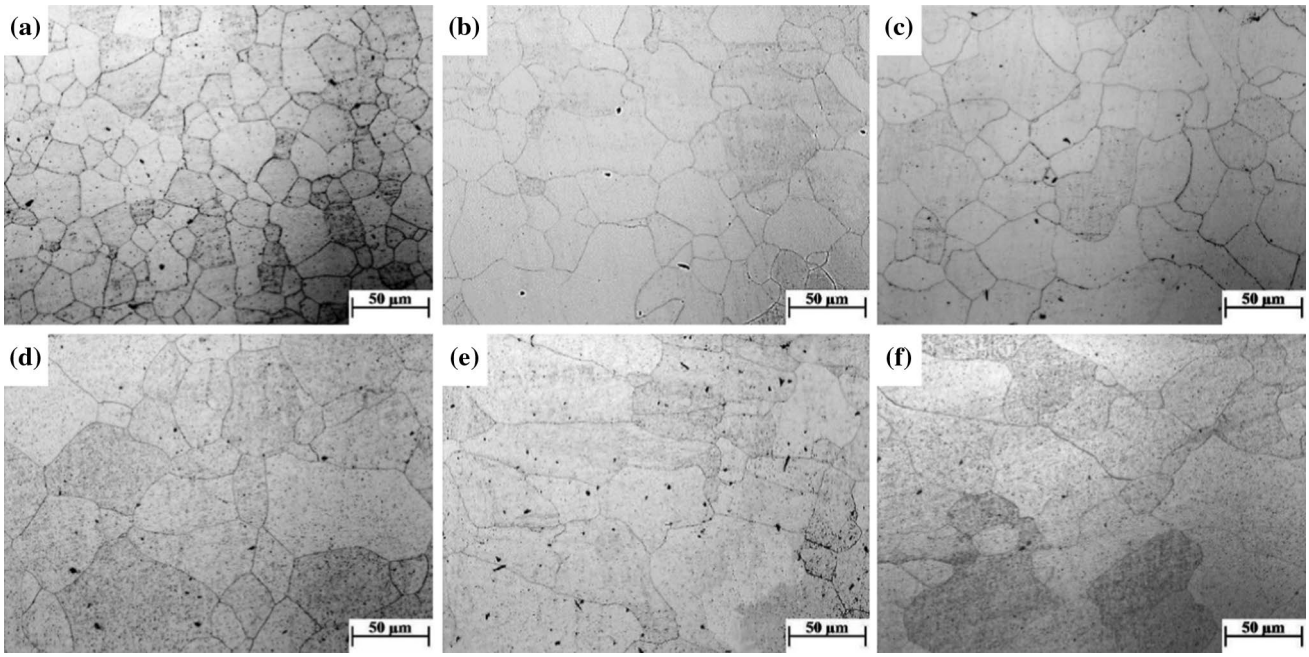

Fig. 2 OM microstructures in three directions of the sheets under different processes: No. 1 **a** ND **b** RD **c** TD; No. 2 **d** ND **e** RD **f** TD

wire-electrode cutting, followed by mechanically grinding to a thickness of about 50 μm. Finally the specimens were electro-polished in a solution of 5% perchloric in ethanol at a temperature below − 20 ºC. The extraction replicas were prepared by evaporating carbon film on the samples which were pre-polished and pre-etc.hed in 4% nital. Then the specimens were immersed in 4% nital to strip the carbon film from the surface. The energy dispersive X-ray spectrum (EDS) in the TEM was used to identify the chemical composition of the precipitates. X-ray diffraction (XRD) analysis was also employed to identify the dislocation density by using X-ray diffractometer (Rigaku TTR-3) with Cuk_a radiation. The diffraction lines were recorded from $2\theta = 40°$ to 100° with a step of 0.01° to cover the diffractions of (110) (200) (211) and (220). Then, the corresponding instrumental width was subtracted from each peak width. In addition, the surface of the specimens were mechanically polished and electropolished and the textures of different samples were determined by Electron Back-Scattered Diffraction (EBSD) using Zeiss EVO-18 scanning electron microscope (SEM).

4 Investigation on the Grain Size Evolution with the Deformation Temperature

Previous studies have focused on the continuous cooling transformation behavior after austenite deformation by using thermo mechanical simulation. The deformation parameters were set based on the actual CSP process. Results showed that the Ar_3 and Ar_1 temperatures were 891 °C and 846 °C, respectively. Then, two passes deformation thermal–mechanical simulation were conducted to further investigate the grain size change with the deformation temperature in γ–α dual phase and α single phase. The deformation temperature after austenite deformation was set as 885 °C, 850 °C, 835 °C, 820 °C, 800 °C and 780 °C. The deformation rate was 40 s^{-1} and the deformation amount was 60%. After deformation, the samples were all quenched to room temperature. Then, the microstructures were observed by OM and the ferrite grain sizes were measured.

5 Results and Discussions

5.1 Microstructural Characterization

5.1.1 OM Microstructure

The OM microstructures of the sheets in different directions were shown in Fig. 2. It can be seen that the microstructures were all full polygonal ferrite while the grain size of the sheet under process No. 1 was much finer than that of process No. 2. For the given process, the microstructures in the normal direction were a little finer than that in other directions. The grain size was given from measuring more than 100 grains. Also, the average sizes of the sheet under different processes were calculated by averaging the size in different directions. The values were all shown in Fig. 3.

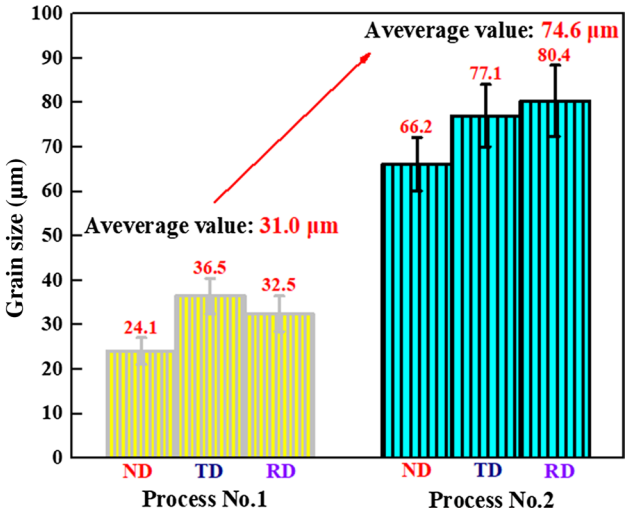

Fig. 3 The grain size of the experimental sheets under different processes

6 EBSD Analysis

The EBSD results which showed the tri-color inverse pole figure map overlapped with grain boundaries can be seen in Fig. 4. The high angle grain boundaries with misorientations larger than 15° were shown by black lines. Each grain with different orientations can be clearly distinguished by the different colors [12]. It can be seen from the Fig. 4a and b which showed the EBSD results of the sheet under process No. 1 that the grains with green color were in the majority in the rolling direction while there were more grains with blue color in the normal direction. That is to say, {111}<110> was the main grain orientation. For process No. 2, EBSD results in Fig. 4c and d showed that the grains with different color in different direction were nearly uniformly distributed. There was no obvious main orientation shown in the grains which may be due to the larger grain size in the field of view. Even so, too large field of view may lead to the loss of calibration rate. Thus, the orientation distribution function (ODF) sections in the Euler space with a constant φ2 = 45° of the sheets were shown in Fig. 5. Figure 5a showed that the textures were broadly distributed in the ODFs of sheets under process No.1 and only the intensity of texture {110}<223> was comparatively stronger than other textures. Inversely, there were three textures with obvious stronger intensities in the ODFs of sheets under process

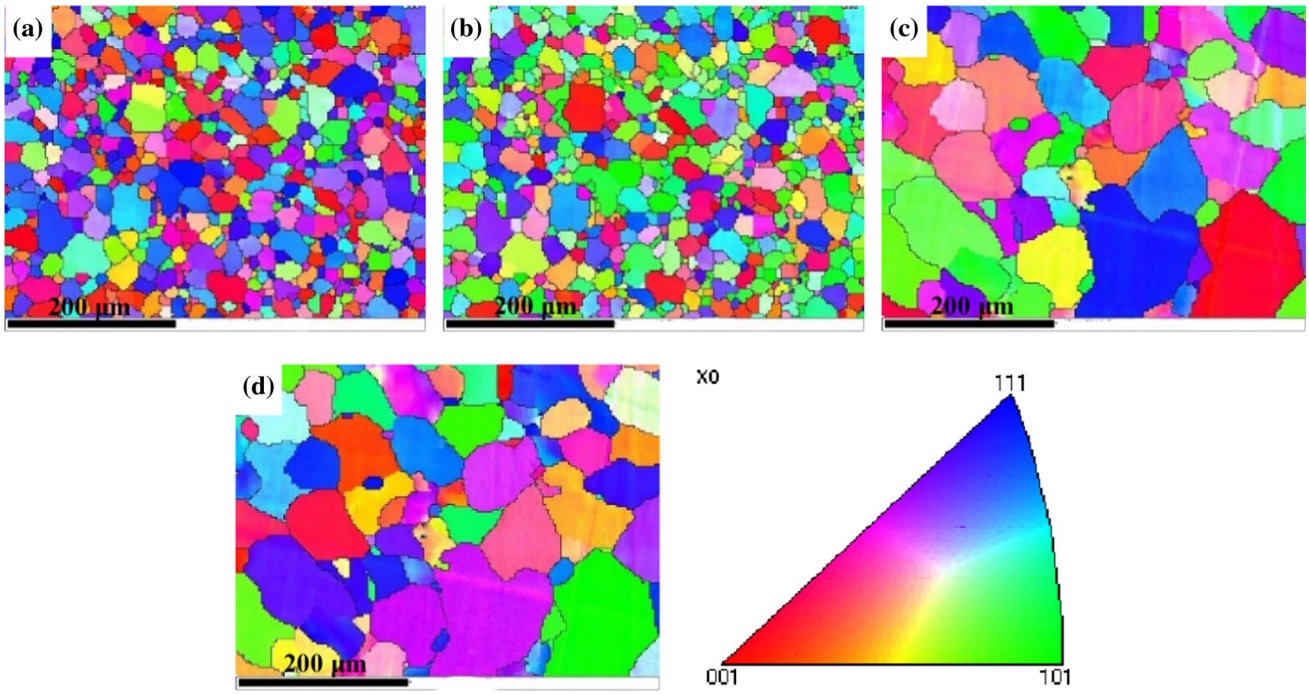

Fig. 4 Tri-color inverse pole figure map overlapped with grain boundaries of the two sheets under different processes: No. 1 **a** rolling direction, **b** normal direction; No. 2 **c** rolling direction, **d** normal direction

Results measured showed that the average ferrite grain size of the sheet under the process No. 2 was nearly two times that of the process No. 1.

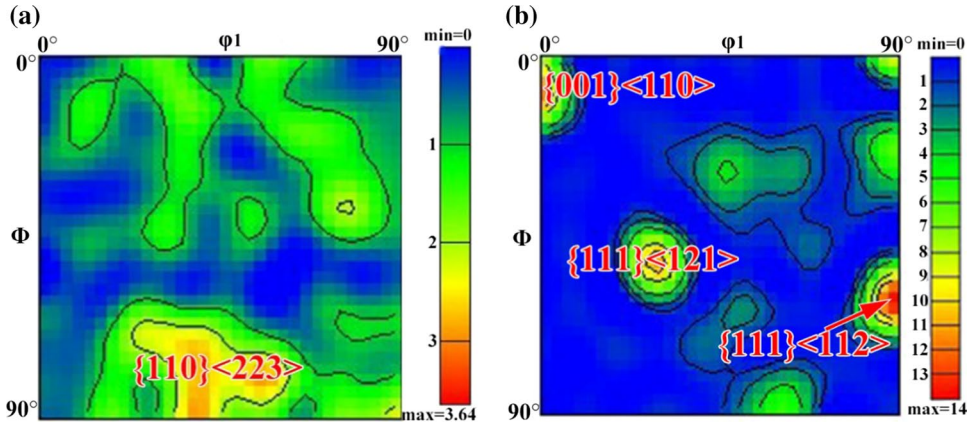

Fig. 5 ODF sections in the Euler space with a constant φ2 = 45° of different processes: **a** No. 1, **b** No. 2

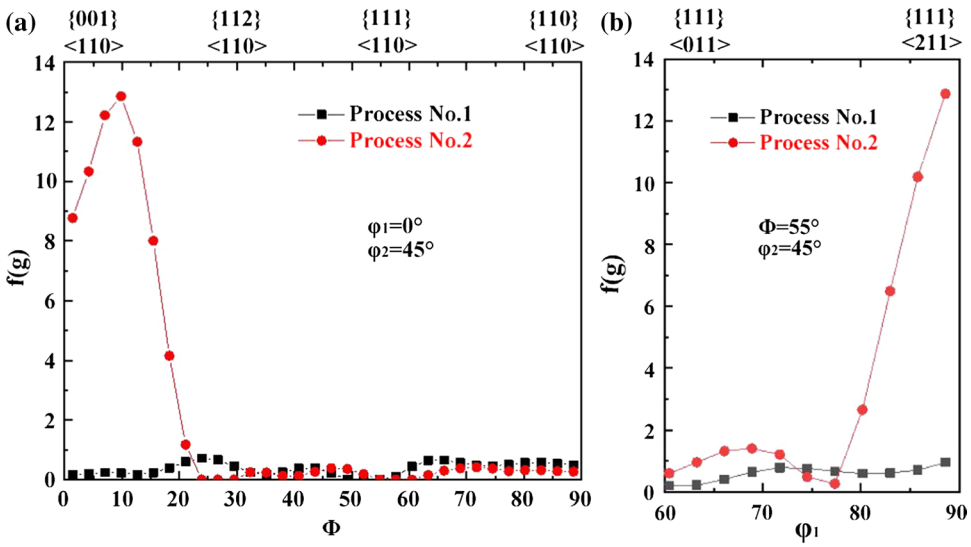

Fig. 6 Orientation density f(g) under different processes: **a** along the α fiber; **b** along the γ fiber

No. 2, {001}<110>, {111}<121> and {111}<112>, as shown in Fig. 5b. The orientation density along the α fiber (<110>// RD) and γ fiber ({111} // ND) as a function of φ1 and Φ were also shown in Fig. 6. For process No. 1, no obvious stronger texture orientation was found in both α and γ fibers. However, a distinct peak of orientation density of texture {001}<110> can be found in α fiber as shown in Fig. 6a and the same thing occurred for the texture {111}<112> in γ fiber as seen in Fig. 6b.

7 TEM Characterization and XRD Analysis

TEM morphology and EDS analysis of the precipitates in the sheets under different processes were shown in Fig. 7 by means of observing the carbon extraction replicas evaporated on the samples. It can be seen in the figure that almost no precipitates were observed in the microstructures of the sheets under different processes. Only very few Ti(C, N) particles was found in the microstructures of the sheet under process No. 2 as shown in Fig. 7b. This could be contributed to the free microalloying composition and the tiny minority of Ti(C, N) particles may form resulting from the residual Ti in the steel. TEM morphology of the microstructures in the sheets under different processes were shown in Fig. 8 by means of observing the thin foil specimens. It can be seen in Fig. 8a that there was dislocations with low density in the microstructure under process No. 1 and a lot of recrystallized grains were also found. However, in the microstructure under process No. 2, higher density dislocation and even sub-grains can be seen, as shown in Fig. 8b, compared with that of process No. 1.

To further quantificationally analyze the dislocation, XRD analysis was employed to obtain dislocation density. XRD peak broadening caused by strain has long been investigated in connection with dislocation density [13, 14]. The XRD peak width, δ_{hkl}, was related to the strain through the following Williamson–Hall (WH) equation [15]. The relationship can be expressed as follows:

$$\delta_{hkl}\frac{\cos\theta_{hkl}}{\lambda} = \frac{0.9}{D} + 2\varepsilon\frac{\sin\theta_{hkl}}{\lambda} \quad (1)$$

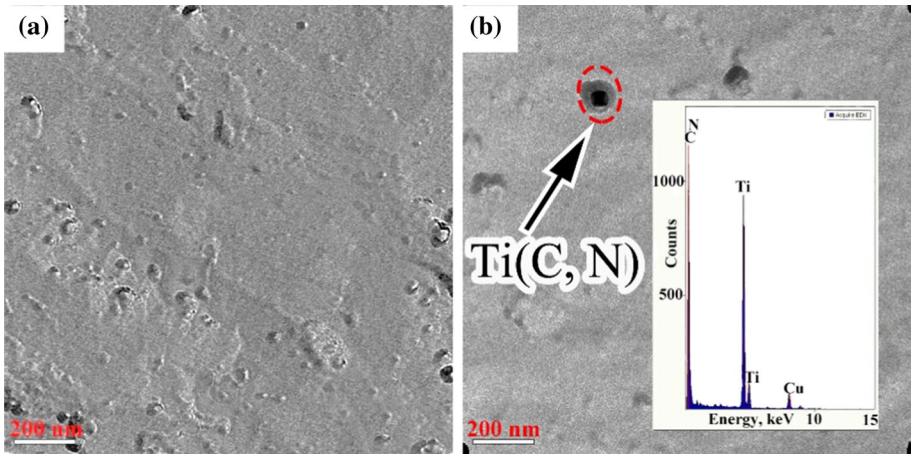

Fig. 7 TEM morphology and EDS analysis of the precipitates in the sheets under different processes: **a** No. 1; **b** No. 2

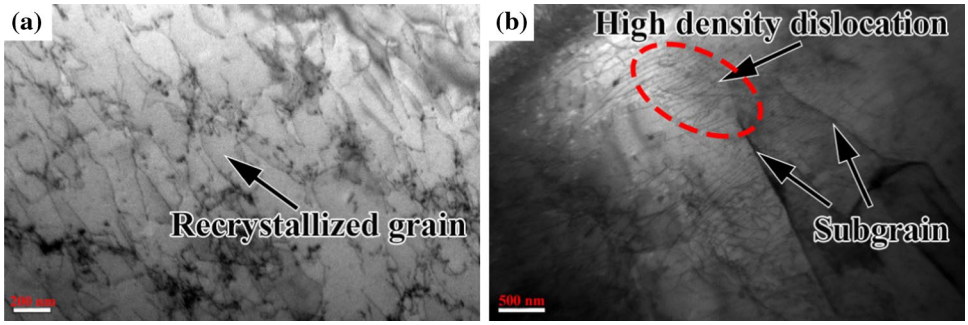

Fig. 8 TEM micrographs of the sheets under different processes: **a** No. 1, **b** No. 2

where θ_{hkl}, ε and D are the diffraction angle, strain and average grain size, respectively. λ is X-ray wave length of copper target which is 0.1542 nm in this experiment, The line width caused by grain size can be neglected when the grain size is larger than 100 nm. δ_{hkl} can also be calculated by the equation below:

$$\delta'^{2}_{hkl} = \delta^{2}_{hkl} + \delta^{0\,2}_{hkl} \tag{2}$$

where δ'_{hkl} is the line width of the deformed specimen; δ^{0}_{hkl} is the standard referenced specimen which was fully annealed in this experiment. ε has a positively related to the dislocation density which can be expressed as follows:

$$\rho = 14.4\frac{\varepsilon^2}{b^2} \tag{3}$$

where b is the magnitude of the Burgers vector, which is 0.248 nm for ferrite. The XRD line profiles of different diffraction peaks of the sheets under different processes were shown in Fig. 9. It can be seen that the diffraction peak {110} has the highest density and became narrower and more intense in the specimen under process No. 2 than that under process No. 1. However, the diffraction peak {211} in the specimen under process No. 1 was a little narrower than that under process No. 2. There were no much difference in width of other diffraction peaks. The widths were all measured by the software as obtained as $\delta'_{hkl.}$ Then, δ_{hkl} can be calculated based on Eq. 2. The value were shown Table 2. Thus, the $\delta_{hkl}\frac{\cos\theta_{hkl}}{\lambda}$ and $2\frac{\sin\theta_{hkl}}{\lambda}$ of the sheets under different processes were obtained for each diffraction angle. After that, the $\delta_{hkl}\frac{\cos\theta_{hkl}}{\lambda}$ was plotted versus $2\frac{\sin\theta_{hkl}}{\lambda}$ as can be seen in Fig. 10. The slopes of the lines for different processes were also marked in the figure. According to Eq. 1, the value of the slope corresponding to the value of the strain ε was obtained. As shown in Fig. 10, the strain ε of processes No. 1 and No. 2 were 0.00052 and 0.00073, respectively. Consequently, based on Eq. 3, the dislocation densities of the sheets under processes No. 1 and No. 2 were also calculated as 6.33×10^{9} cm^{-2} and 1.25×10^{10} cm^{-2}, respectively. The quantificative results of the dislocation density by XRD analysis was unanimous to the TEM observation.

8 Mechanical Properties

8.1 Softening Mechanism of Ultra-Low Carbon Steel

The Mechanical properties in different sampling directions of the sheets under different processes were shown in Table 3. Also, the average values of different properties

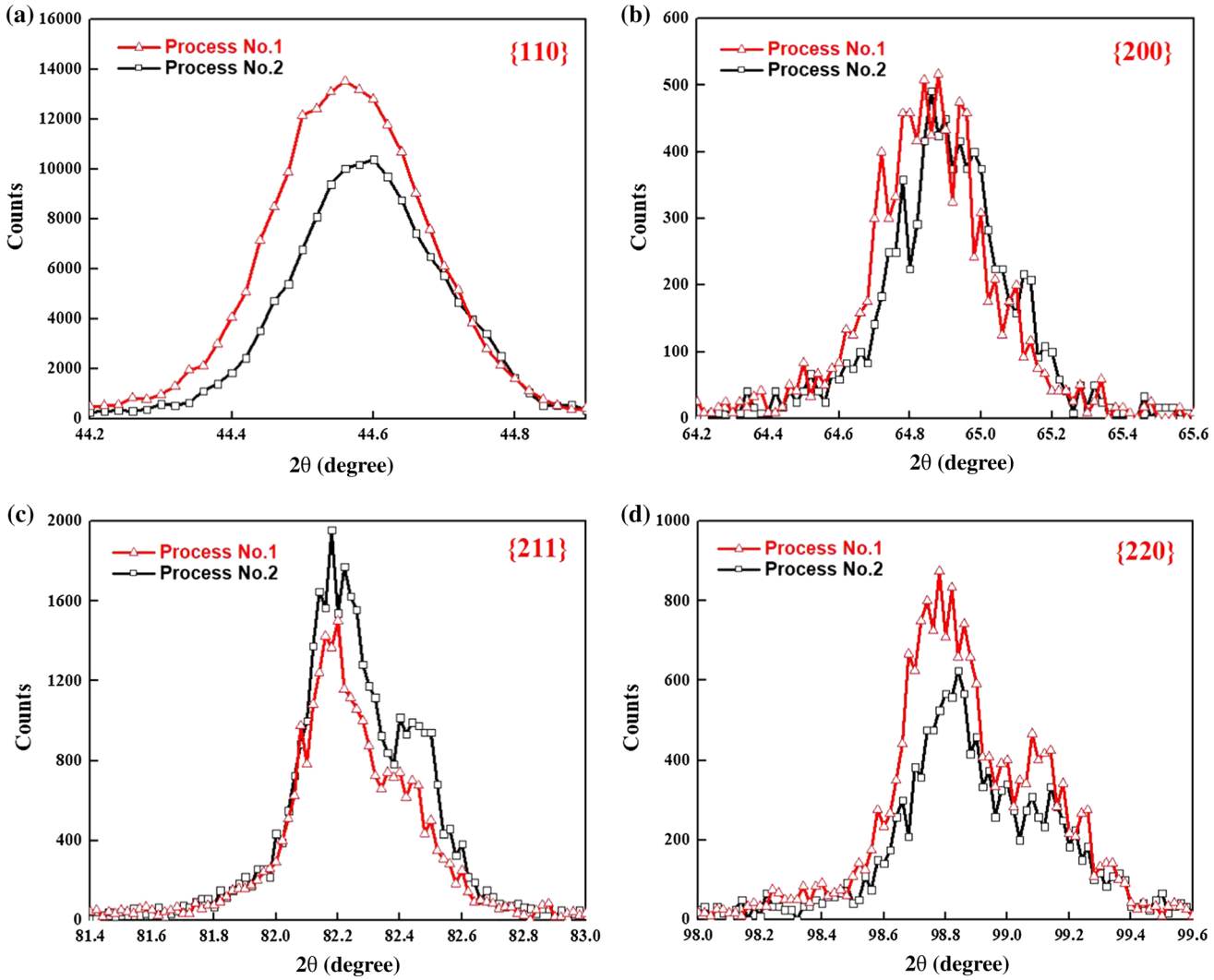

Fig. 9 XRD peaks of the sheets under different processes. **a**, **b**, **c** and **d** correspond to (110) (200) (211) and (220) diffraction peaks, respectively

Table 2 The peak width of the experimental sheets at different diffraction peaks

Process no.	The peak width δ_{hkl}, nm^{-1}			
	{110}	{200}	{211}	{220}
No. 1	0.242	0.327	0.325	0.387
No. 2	0.230	0.322	0.335	0.387

were given by averaging the values in three directions. It can be seen that there were small variations of mechanical properties in different directions for a given hot sheet. By comparing the two processes, the sheet under process No. 1 had a slightly higher yield and tensile strength while had a 6.3% higher elongation than that of the sheet under process No. 2. Previous researches showed that the elongation of low carbon steel was insensitive to the grain size while changed with the dislocation density [16–18]. It has been shown that the elongation did not change with the grain size because the refinement of grain can both increase the flow stress and the work hardening rate thus does not affect the uniform strain. The mobility of dislocation was reduced when the dislocation density increased because of the interaction between the dislocations. Then, the plastic deformation ability became weaker and the uniform elongation was reduced [18]. The yield strength of ferritic steel has been often contributed by many factors including solid solution strengthening, grain boundary strengthening, dislocation strengthening and precipitation strengthening [19–22]. For the same steel, the solid solution strengthening factors of the sheets under Processes No. 1 and No. 2 can be regarded as the same. For identifying the yield strength contributed by grain boundary strengthening, the Hall-Patch equation has often been used as the follows:

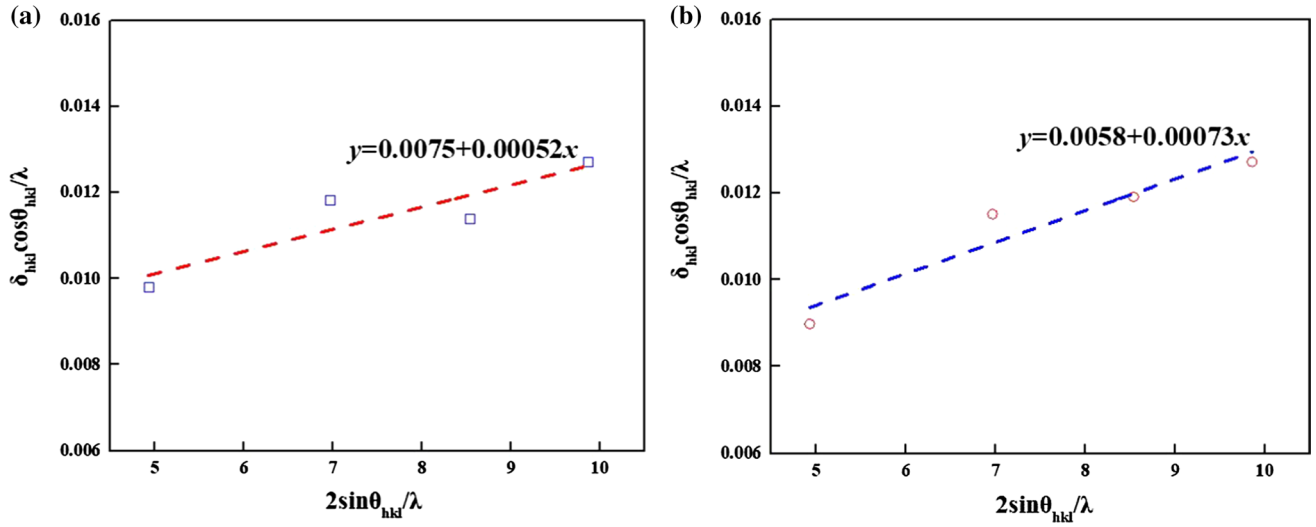

Fig. 10 The $\delta_{hkl}\frac{\cos\theta_{hkl}}{\lambda}$ versus $2\frac{\sin\theta_{hkl}}{\lambda}$: **a** process No. 1, **b** process No. 2

Table 3 Mechanical properties in hot rolled sheets under different processes

Process no.	Sampling direction	Yield strength (MPa)	Tensile strength (MPa)	Elongation (%)	r	△r	r̄
No. 1	RD	232	321	39.5	0.89	− 0.02	0.95
	45°	229	321	37.7	0.97		
	TD	229	326	37.8	0.97		
	Average value	230	323	38.3	0.94		
No. 2	RD	213	295	32.5	1.19	0.07	1.01
	45°	224	305	31.9	0.93		
	TD	220	310	31.5	0.98		
	Average value	219	303	32.0	1.03		

$$\sigma_G = k_G D^{-1/2} \tag{4}$$

where k_G is the Hall–Petch coefficient and D is the the grain size of ferrite. k_G was nearly 18.1 MPa $mm^{1/2}$ [16, 23]. It can be seen in Fig. 3 that the average grain sizes of ferrite of the sheets under processes No. 1 and No. 2 were 31.0 μm and 74.6 μm, respectively. Thus, the yield strengths of the sheets under processes No. 1 and No. 2 contributed by grain boundary strengthening were calculated as 103 MPa and 66 MPa, respectively. Consequently, the yield strength difference of the sheets under two different processes contributed by the grain size difference was approximately 37 MPa. The dislocation strengthening factor σ_d was often expressed as the following equation:

$$\sigma_d = M\alpha\mu b\rho^{1/2} \tag{5}$$

where M is the orientation factor which is 3.1 for α-Fe; α is a proportional coefficient set as 0.15; μ is the shearing factor and is 8.26×10^4 MPa for ferritic steels; b is the Burgers vector of ferrite and equals to 0.248 nm; ρ is the dislocation density and the values of the sheets under processes No. 1 and No. 2 were calculated as 6.33×10^9 cm^{-2} and 1.25×10^{10} cm^{-2}, respectively. Consequently, the yield strengths of the sheets under processes No. 1 and No. 2 contributed by dislocation strengthening were calculated as 76 MPa and 106 MPa, respectively. The yield strength contributed by dislocation strengthening of the sheet under process No. 2 was 30 MPa higher than that of the sheet under process No. 1. Since the yield strength difference of the sheets under two different processes contributed by the grain size difference was 37 MPa, it can be inferred that the yield strength difference was decreased to 7 MPa by the dislocation strengthening. For the precipitation strengthening, it is often influenced by the diameter and the volume fraction of precipitates which can be explained by Ashby–Orawan equation [16, 20]. However, almost no precipitate was found in the microstructures of the sheets under different processes. Thus, the contributions to the yield strength difference by the

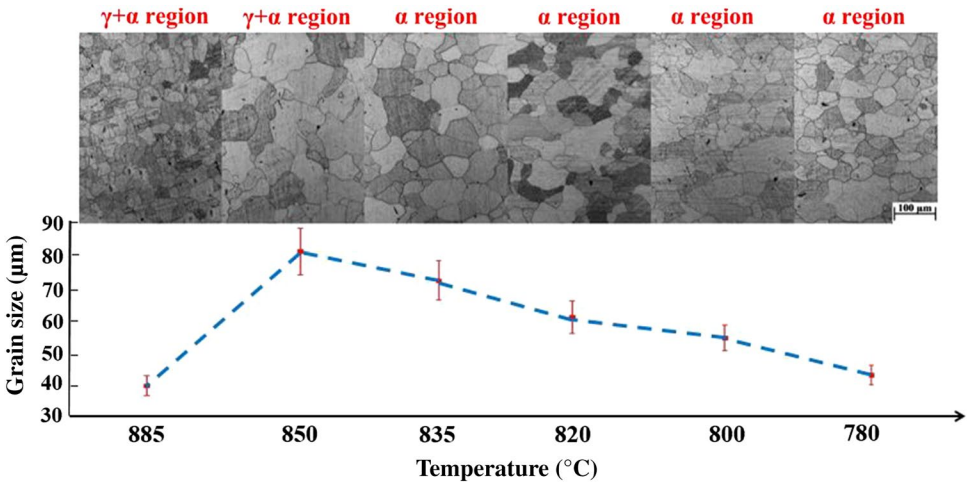

Fig. 11 The grain size evolution with the deformation temperature

precipitation strengthening could be nearly regarded as zero. By comparing the measured yield strength difference as can be calculated as 11 MPa in Table3, the calculated value fitted well with the measured value. In short, the softening mechanism of the experimental sheet was the coarsening of ferrite grain.

9 Effect of Texture Changes on the Formability

For the formability, it can be seen in Table3 that the average r value and $\bar{r}$ value in the sheet under process No. 2 were 0.09 and 0.06 higher than that in the sheet under process No. 1, respectively. The anisotropic coefficient Δr values of the sheets under different processes were both close to zero which showed a good similarity of formability in different directions. The $\bar{r}$ and Δr values were closely related to the texture formed in the sheet [9]. It has been well known that the development of strong {111} recrystallization textures could ensure high mean r values and, hence, good formability of steel sheets [5, 24]. In addition to the favorable {111} component, the textures also included a higher density of {001} orientation which can be seen Fig. 7a. This was unanimous to the previous reports which showed that there existed {001}<110> component when rolling at higher temperature of ferrite region [7]. Previous studies also showed that {001} orientation was detrimental to the formability. Also, it was found that the shear bands formed during deformation presented to nucleate a strong {111} texture and the population of shear bands decreased as the rolling temperature was increased [5–7, 24]. Consequently, the combined role of {001} and {111} orientation resulted in a slight increase of the r and $\bar{r}$ value in the sheet under process No. 2.

10 Effect of Deformation Temperature on the Microstructure and the Process Control Strategy in CSP Process

It was concluded above that the softening of the sheets under process No. 2 could be attributed to the grain coarsening of ferrite and the reduction of elongation was due to the dislocation strengthening. Also, the dislocation strengthening could increase the strength of the sheets under process No. 2. Consequently, the grain size should be further increased and the dislocation strengthening should be eliminated in order to further decrease the strength and increase the elongation. In Fig. 1, it can be seen that the biggest difference in the process between No. 1 and No. 2 was the rolling temperatures. The microstructure evolution with the deformation temperature was shown in Fig. 11 in order to analyze the effect of rolling temperature. The temperature 885 °C fell into the higher temperature stage of γ-α dual phase region and the temperature 850 °C was in the lower temperature stage of γ-α dual phase region. The other temperatures were in α single phase region. It can be seen in Fig. 11 that the ferrite grain was the finest at the temperature of 885 °C while became abnormally coarser at the temperature of 850 °C. The grain size then gradually decreased with the temperature decreasing in α single phase region. As reported, the refinement mechanism of austenite or ferrite deformation was related to the recrystallization behavior which was driven by the stored energy [10, 25–27]. Thus, the grain sizes were all refined when the deformation occurred in the higher temperature stage of γ-α dual phase region or α single phase region because of the austenite and ferrite recrystallization. According to previous studies [28, 29], the $\gamma \rightarrow \alpha$ transformation was an energy driving process. Consequently, there was less driving force for the recrystallization when the deformation was in the lower temperature stage of γ-α dual phase region because the energy was consumed by the phase transformation. Thus, the transformed strain-free ferrite grains grew to

the surrounding deformed ferrite grains during cooling and coiling [9]. This meant that grain growth of strain-free ferrite occurred in this region and also the grain size increased with the temperature decreasing. The maximum grain size could be obtained when the deformation was conducted near to the Ac_1 temperature. In addition, many reports have focused on the dislocation formation during deformation and showed that lowering the deformation temperature could increase the dislocation density [6, 10, 27]. Also, it has well known that the coiling temperature has a great influence on the dislocation density after coiling. Higher coiling temperature will promote the recrystallization of steel and thus reduce the dislocation density. Even so, the dislocation density in the sheet under process No. 2 with higher coiling temperature was still higher than of the sheet under process No. 1 with lower coiling temperature. It can be concluded that the deformation temperature has a stronger influence on the dislocation density than the coiling temperature. Consequently, deformation at the Ac_1 temperature in CSP process was a wise choice because it could not only increase the grain size but also decrease the dislocation density. Then, the strength of the sheets could be further reduced and the elongation could also be improved.

11 Conclusions

(1) The average ferrite grain sizes of austenite rolling sheet and multiphase rolling sheet were 31.0 μm and 74.6 μm, respectively. There were three textures with obvious stronger intensities in the ODFs of sheet after multiphase rolling, {001}<110>, {111}<121> and {111}<112>. The dislocation density of austenite rolling sheet was 6.33×10^9 cm^{-2} while that of multiphase rolling sheet was increased to 1.25×10^{10} cm^{-2}.

(2) The sheet after austenite rolling had a slightly higher yield and tensile strength while had a 6.3% higher elongation than that of the sheet after multiphase rolling. The higher dislocation in the sheet after multiphase rolling increased the strength while decreased the elongation. The softening mechanism of the sheet after multiphase rolling was the coarsening of ferrite grain.

(3) The average r value and $\bar{r}$ value in the sheet after multiphase rolling were 0.09 and 0.06 higher than that in the sheet after austenite rolling, respectively. The combined role of {001} and {111} orientation resulted in a slight increase of the r and $\bar{r}$ value in the sheet after multiphase rolling.

(4) The maximum grain size could be obtained when the rolling was conducted near to the Ac_1 temperature. It was a wise choice to conduct rolling at the Ac_1 temperature in CSP process to increase the grain size and decrease the dislocation density. Then, the strength of the sheets could be further reduced and the elongation could also be improved.

Acknowledgements The authors appreciate the financial support by the National Natural Science Foundation of China (No. 51701015).

References

1. R. Kaspar, Microstructural aspects and optimization of thin slab direct rolling of steels. Steel Res Int **74**(5), 318–326 (2003)
2. C. Klinkenberg, C. Bilgen, T. Boecher et al., 20 years of experience in thin slab casting and rolling state of the art and future developments. Mater Sci Forum **638**, 3610–3615 (2010)
3. B. Gardiola, M. Humbert, C. Esling et al., Determination and prediction of the inherited ferrite texture in a HSLA steel produced by compact strip production. Mater Sci Eng, A **303**(1–2), 60–69 (2001)
4. X. Zhu, G. Zhu, W. Mao, Comparison of grain size in plain carbon hot-rolled sheets manufactured by CSP and conventional rolling processing. J Iron Steel Res Int **19**(1), 17–22 (2012)
5. M.R. Toroghinejad, F. Ashrafizadeh, A. Najafizadeh et al., Effect of rolling temperature on the deformation and recrystallization textures of warm-rolled steels. Metall Mater Trans A **34**(5), 1163–1174 (2003)
6. M.R. Barnett, J.J. Jonas, Influence of ferrite rolling temperature on microstructure and texture in deformed low C and IF steels. ISIJ Int **37**(7), 697–705 (1997)
7. M.R. Barnett, J.J. Jonas, Influence of ferrite rolling temperature on grain size and texture in annealed low C and IF steels. ISIJ Int **37**(7), 706–714 (1997)
8. S. Matsuoka, K. Sakata, S. Satoh et al., Effect of hot-rolling strain rate in the ferrite region on the recrystallization texture of extra-low C sheet steels. ISIJ Int **34**(1), 77–84 (1994)
9. W.C. Jeong, Effect of hot-rolling temperature on microstructure and texture of an ultra-low carbon Ti-interstitial-free steel. Mater Lett **62**(1), 91–94 (2008)
10. D. Liu, A.O. Humphreys, M.R. Toroghinezhad et al., The deformation microstructure and recrystallization behavior of warm rolled steels. ISIJ Int **42**(7), 751–759 (2002)
11. GB/T 228–2010, Metallic Materials-Tensile Testing-Part 1: Method of Test at Room Temperature, 2011. Beijing, China.
12. C. Wang, M. Wang, J. Shi et al., Effect of microstructural refinement on the toughness of low carbon martensitic steel. Scripta Mater **58**(6), 492–495 (2008)
13. S. Takebayashi, T. Kunieda, N. Yoshinaga et al., Comparison of the dislocation density in martensitic steels evaluated by some X-ray diffraction methods. ISIJ Int **50**(6), 875–882 (2010)
14. J. Pešička, R. Kužel, A. Dronhofer et al., The evolution of dislocation density during heat treatment and creep of tempered martensite ferritic steels. Acta Mater **51**(16), 4847–4862 (2003)
15. M. Li, L. Wang, J.D. Almer, Dislocation evolution during tensile deformation in ferritic–martensitic steels revealed by high-energy X-rays. Acta Mater **76**, 381–393 (2014)
16. B.C. De Cooman, J.G. Speer, *Fundamentals of Steel Product Physical Metallurgy* (AIST, Association for Iron & Steel Technology, Warrendale, 2011)
17. B. Jiang, M. Wu, M. Zhang et al., Microstructural characterization, strengthening and toughening mechanisms of a quenched and tempered steel: effect of heat treatment parameters. Mater Sci Eng, A **707**, 306–314 (2017)

18. Q. Yong, *Second Phases in Structural Steels* (Metallurgical Industry Press, Beijing, 2006). **(in chinese)**
19. B. Jiang, Z. Mei, L. Zhou et al., Microstructure evolution, fracture and hardening mechanisms of quenched and tempered steel for large sized bearing rings at elevated quenching temperatures. Met Mater Int **22**(4), 572–578 (2016)
20. T. Hao, Z.Q. Fan, S.X. Zhao et al., Strengthening mechanism and thermal stability of severely deformed ferritic/martensitic steel. Mater Sci Eng, A **596**, 244–249 (2014)
21. L. Rancel, M. Gómez, S.F. Medina et al., Measurement of bainite packet size and its influence on cleavage fracture in a medium carbon bainitic steel. Mater Sci Eng, A **530**, 21–27 (2011)
22. P. Yan, Z. Liu, H. Bao et al., Effect of normalizing temperature on the strength of 9Cr–3W–3Co martensitic heat resistant steel. Mater Sci Eng, A **597**, 148–156 (2014)
23. Y. Kang, H. Yu, K. Wang et al., Study of microstructure and strengthening mechanism of low carbon steel produced by CSP line. Iron Steel **38**(8), 20–25 (2003). **(in chinese)**
24. M.R. Barnett, role of in-grain shear bands in the nucleation of <111>//ND recrystallization textures in warm rolled steel. ISIJ Int **38**(1), 78–85 (1998)
25. C.L. Miao, C.J. Shang, H.S. Zurob et al., Recrystallization, precipitation behaviors, and refinement of austenite grains in high Mn, high Nb steel. Metall Mater Trans A **43**(2), 665–676 (2012)
26. A. Najafi-Zadeh, S. Yue, J.J. Jonas, Influence of hot strip rolling parameters on austenite recrystallization in interstitial free steels. ISIJ Int **32**(2), 213–221 (1992)
27. S.V.S.N. Murty, S. Torizuka, K. Nagai et al., Dynamic recrystallization of ferrite during warm deformation of ultrafine grained ultra-low carbon steel. Scripta Mater **53**(6), 763–768 (2005)
28. S.C. Hong, S.H. Lim, K.J. Lee et al., Effect of undercooling of austenite on strain induced ferrite transformation behavior. ISIJ Int **43**(3), 394–399 (2003)
29. C.J. Huang, D.J. Browne, S. McFadden, A phase-field simulation of austenite to ferrite transformation kinetics in low carbon steels. Acta Mater **54**(1), 11–21 (2006)